Contribution of dynamic capillary pressure to rainfall infiltration in thin homogeneous growth substrates

Journal of Hydrology 603 (2021) 126851

Contents lists available at ScienceDirect

Journal of Hydrology

journal homepage: www.elsevier.com/locate/jhydrol

Contribution of dynamic capillary pressure to rainfall infiltration in thin homogeneous growth substrates

Kaj Pettersson [a,*], Dario Maggiolo [b], Srdjan Sasic [b], Pär Johansson [a], Angela Sasic Kalagasidis [a]

[a] Dpt.Architecture & Civil Engineering, Chalmers University of Technology, Chalmersplatsen 4, 412 96 Göteborg, Sweden
[b] Dpt. Mechanics & Maritime Sciences, Chalmers University of Technology, Chalmersplatsen 4, 412 96 Göteborg, Sweden

ARTICLE INFO

This manuscript was handled by C. Corradini, Editor-in-Chief, with the assistance of Philip Brunner, Associate Editor

Keywords:
Green roof
Microstructure
Porous media
Dynamic capillary pressure
lattice Boltzmann

ABSTRACT

The use of green roofs to help mitigate storm water contributions to urban flooding has been gaining popularity but is hindered by the limited data on the performance of such roofs with regard to storm water runoff mitigation. The underlying issue stems from the inherent complexity of modeling subsurface multiphase flow. Modeling of this phenomena requires calculating the contributions of substrate microstructure characteristics, the influence of the wetting and non-wetting phases upon each other, and the effect of the microstructure on the wetting phase. Previously we have observed how the microstructure can affect detention, however the quantification of this relationship is still missing. In the present paper we present numerical simulations of wetting phase infiltration of a thin monodisperse packed bed in order to understand and quantify the impact of microstructure geometry on storm water infiltration of a green roof substrate. For a slightly hydrophilic case, ($\theta = 82^{\circ}$), we find that a dominant mechanism underlying this relationship is the microstructure-induced dynamic behavior of the capillary pressure. We determine that at larger packing ratios (ratio of packed bed depth to particle size), the influence of hydraulic head diminishes and behaves conversely for thinner layers, particularly when larger pores are present. Indeed, thin beds composed of large particles can exhibit high flow velocities that in turn affect the capillary pressure within the substrate. We observe that the capillary pressure can shift from negative values denoting capillary suction to positive ones which cause valve-like blocking effects on the flow; dependent upon the flow velocity as determined by the microstructure. In particular, we find that the capillary pressure depends on the value of the pore-scale gravity-induced flow velocity, quantified through a characteristic Capillary number. The provided quantification of this relationship can be invaluable from a design perspective to understand the behavior of capillary pressure of different substrates under a variety of flow rates prior to testing substrate candidates. In addition, a comparison of the behavior of the dynamic component of capillary pressure to other works is undertaken. Flow homogeneity is also found to be linked to the flow velocity, and consequently to the microstructure.

1. Introduction

With the predicted increase in precipitation frequency and intensity in northern latitudes and the current issues regarding urban storm water management, green roofs have emerged as an attractive technology for urban areas (Bliss et al., 2009). Green roofs are defined as any roof construction incorporating vegetation, usually accompanied by additional layers of growth substrate, drainage, and waterproofing. The primary driving forces for green roof usage are their ability to reduce peak storm water runoff loads through retention of water in the soil and vegetation as well as detention through mechanical processes within the soil or alternative drainage layer (Johannessen et al., 2017). The term retention refers to the entrapment of liquid within the drainage layer as well as in the vegetation and is removed through evapotranspiration. Detention is defined as the ability of the drainage and vegetation layers to impede liquid infiltration and drainage, thus lowering the peak flow intensity and lengthening the drainage period. Much research has been done both experimentally and using a variety of modeling approaches to accurately quantify these benefits. While experiments have been able to provide information regarding the hydrological performance of different layering designs and types of vegetation under both laboratory and *in situ* conditions, accurately capturing the behavior from the modeling

* Corresponding author.
E-mail address: kajp@chalmers.se (K. Pettersson).

https://doi.org/10.1016/j.jhydrol.2021.126851
Received 16 December 2020; Received in revised form 14 August 2021; Accepted 17 August 2021
Available online 25 August 2021

perspective has remained elusive.

Typically, the computational methods used to evaluate the hydrological performance of green roofs are taken from soil science and those used in the petrochemical industry. These models at the macroscopic scale are directly based upon the Richards equation for unsaturated flow or a multiphase model derived from Darcy's law. They require additional equations in order to describe the relationship between the wetting and non-wetting phases, in the simplest case water and air or water and oil, as well as the solid–liquid interactions. This inter-relationship has been the subject of widespread academic research for the better half of a century largely due to the complexity of the physical process and consequent challenges in predicting the behavior of the system during both infiltration and drainage. The complexity is appreciably increased when ones considers the variability in geometrical characteristics that define the microstructure of a porous medium.

In most works on the topic of flow through porous media, be it at the macroscopic or microscopic scale, require a few fundamental definitions, provided here. The relationship between the liquid phases and the solid porous matrix is commonly formalized by the equations relating capillary pressure, saturation, and permeability. Capillary pressure p_c is defined as the difference between the wetting and non-wetting liquid pressures, p_w and p_{nw} respectively, calculated on either side of the phasic interface:

$$p_c = p_w - p_{nw}. \tag{1}$$

Saturation is given by the total wetting phase present in the porous matrix within a defined volume over the total void space within that volume. Permeability is a measure of the ability of a liquid to penetrate a porous matrix and is comprised of an intrinsic (or absolute) permeability as well as a relative permeability. Intrinsic permeability is a property of the material and is calculated by the single phase flow through the porous medium whereas relative permeability is a measure of the effect a wetting and non-wetting phase apply to each other within the porous network. Unsurprisingly, relative permeability is difficult to quantify as it relies on the amount of each phase present locally and may not be spatially homogeneous. In addition, the effect of dynamic contact angles, defined to be different on the advancing and retreating sides of the wetting phase, adds another layer of complexity. It is precisely these difficulties that hinder modeling of this phenomenon for both imbibition and drainage processes in a unified manner. We provide a discussion of previous works using a variety of approaches to better connect the work presented in this paper with the larger field of study.

1.1. Previous research

One aspect of the transport of heat and fluids within a porous network that is not inconsequential is the contribution of evaporation. Though not the first, Luis Segura identified evaporation as a contributing factor in the drying or pore networks by solving flow driven by evaporation and pressure-gradient forces over a simplistic network. He determined that as the drying process progressed the primary driving force shifted from pressure-gradient at higher liquid saturation to evaporative-dominant behavior at lower saturation values (Segura, 2007). Shokri et al. examined the influence on partially wetted porous media and showed that hydrophilic media allow for larger rates of evaporation than in hydrophobic media (Shokri and Lehmann, 2009). They also determined that initial evaporation is driven by capillary-induced flow whereas vapour diffusion dominates in later stages of the process, confirming prior observations. Shahraeeni and Or investigated the effect of liquid bridges on vapor diffusion as a mechanism for evaporation and confirmed previous works that as saturation increases the vapor diffusion is dominated by capillary action within the networks as postulated by Philip and deVries earlier. They also showed that inducing a mild thermal gradient in the vapor phase almost doubly increases the flux when compared to an inert vapor phase (Shahraeeni and Or, 2012). We mention this contribution due to its proven relevance to fluid transport in porous however within this work we consider an isothermal system, and thus evaporation is neglected.

The processes of drainage and imibibition have long been observed to behave dissimilarly with regard to the changes in permeability and saturation, as well as other properties of the flow and soil matrix. This difference, known as hysteresis, is caused by the interactions of the liquid phases with each other as well as the solid matrix morphology and physical properties. This phenomenon has led many researchers to attempt to determine alternative formulations that that of the most common empirical models which make use of the relationship between permeability, capillary pressure, and saturation to describe this process. These models; such as the van Genuchten (1980), Purcell (1949), and Brooks and Corey (1964) require experimental data with which to fit the curves for a complete description of the hysteresis to be generated. A good overview of these models is given by Li and Horne (2006). Experimental approaches to generate the required data vary; with Wayllace and Lu (2012) presenting a novel transient water release and imbibition (TWRI) method to rapidly capture the soil–water retention curve (SWRC) and hydraulic conductivity function under both drying and wetting conditions. Gallage et al. used dual liquid tensiometers to validate their accuracy for sandy soils (Gallage et al., 2013). Soltani et al. carried out a statistical analysis of model parameters in order to generate SWRC curves for different soil classes rather than individual experimental datasets, removing direct subjectivity of the resulting curves (Soltani et al., 2019). Siltecho et al. provide an overview of many of the experimental methods and outline their respective strengths and weaknesses (Siltecho et al., 2015).

As an alternative to the use of empirical functions to close the problem at a macroscopic level, many other researchers have attempted to find additional parameters linked to the ones previously mentioned in order to better explain the physical process and allow for a bijective function to describe the changes. This requires the direct solution of the flow at the pore-scale, and several numerical methods are used for this purpose. The lattice Boltzmann method (LBM) has been used extensively for this purpose due to its inherent advantages: i) its ease of coding, ii) the ease of parallelization for quick computing, iii) and its ability to handle complex boundaries commonly found in porous media. Work by Li et al. described the influence of geometrical properties on steady state fluid distribution and capillary pressure in a variety of 2D porous matrices (Li et al., 2018). Suh et al. examined the effect of irregularly shaped pore throats on the capillary pressure within the matrix and concluded the use of the Mayer and Stowe-Princen theory in lieu of the traditional Young–Laplace approach provides good agreement with experimental data (Suh et al., 2017). Porter et al. undertook an examination of the influence of interfacial area in addition to the capillary pressure–saturation interaction and determined that its inclusion as a variable in such models removes the need for scanning curves to accurately represent the hysteretic nature of the imbibition-drainage process (Porter et al., 2009). Schlüter et al. investigated the validity of using an Euler characteristic as a measure of the fluid topology to determine the aforementioned interactions and compared the results to experimental data with good agreement (Schlüter et al., 2016). Liu et al. employed a similar technique to quantify pore structure influence on capillary flow (Liu et al., 2017). Landry et al. determined the effect of homogeneous-wet and mixed-wet porous media on permeability and found results in line with experimental data regarding the trends of the fluid–fluid and fluid–solid interfaces (Landry et al., 2014).

Li et al. employed a FEM approach with a zero-thickness interface element to solve unsaturated flow in fully 3D porous media (Li et al., 2017). The results showed accurate capturing of the wetting front as well as flow velocity and pressure distribution within the network. Several researchers have opted to solve the Navier–Stokes equations directly at the pore scale: Amiri and Hamouda investigated the influences of viscosity, capillarity, wettability, and heterogeneity on flow in 2D porous media by solving a non-isothermal system using FEM and the Navier–Stokes equations coupled with the phase-field method

(Akhlaghi Amiri and Hamouda, 2014). A similar methodology was employed by Janetti et al. to quantify the effect of pore-scale geometry and wettability on permeability in ordered and random elementary cells (Janetti et al., 2017). The impact on permeability in regular cells was found to be caused by the wettability of the solid whereas in random cells the contribution of geometry was found to be paramount. Ferrari et al. made use of the volume-of-fluid (VOF) method to investigate fingering length and width as well as interfacial area evolution in 2D and 3D settings (Ferrari et al., 2015).

Jeff Gostick and fellow researchers have developed an open source pore network modeling software (OpenPNM) (Gostick et al., 2016) and tested its efficacy against direct numerical solvers such as FEM and LBM methods. The results showed that for the computational expenditure the more simplistic pore network models provide good accuracy, dependent upon discretization schemes used (Sadeghi et al., 2020). The models are based upon the advection–diffusion equation but incorporate the use of power-law and hybrid finite difference schemes as well as the analytical solution to the 1D advection–diffusion equation. Vogel et al. (2005) performed a comparison between a pore-network model, a lattice Boltzmann approach, and a continuum model on determining the soil–water retention curve and found the pore network model to be the best option for cost. The limitation of the lattice Boltzmann method was the regularized lattice which had difficulty capturing thin films within the pores. Primkulov et al. (2019) introduced a "moving capacitor" pore network model which models the fluid–fluid interfaces as moving capacitors within the more traditional pore network model fixed resistor approach. This model allows the capturing of displacement patterns and the injection pressure signal under a larger variety of capillary numbers and wettabilities. Qin et al. have shown that multiform idealized pore elements used in pore network modeling, in combination with the Young–Laplace equation, result in an over-prediction of the capillary force at the wetting front. This result in an over-prediction of the imbibition rate (Qin and van Brummelen, 2019).

The hysteresis in the advancing and retreating contact angle has also been studied in detail, with researchers aiming to fully resolve the physics occurring along the moving contact line. Raiskinmäki et al. simulated capillary rise using lattice Boltzmann and determined a dependence of the contact angle on capillary number as well as a more complex behavior in the presence of gravity (Raiskinmäki et al., 2002). Several other researchers have provided a thorough explanation of the behavior reported in Raiskinmäki et al. and fully described capillary rise in a cylinder of constant diameter in mathematical terms. This detailed description can be found in such works as Athukorallage and Iyer (2016) and Mikelić (2003). Similar derivations have been shown for two-phase flow in a thin strip of variable width as an analogue to idealized porous media. The derivation results in a Darcy-like formulation with a capillary pressure–saturation relation including dynamic effects. This derivation made use of the mathematical technique known as homogenization (Lunowa et al., 2021), similarly to Mikelić. Benzi et al. studied the behavior of the contact angle through the modification of two parameters within lattice Boltzmann: the equivalent of the wall density and the wall-fluid potential as in molecular dynamics (Benzi et al., 2006) and compared the results to experimental data with good agreement. Sbragaglia et al. determined a critical capillary number for wherein the interface shifts from stationary to non-stationary within a Couette flow. They also compared sharp interface models to diffuse ones and determined a limit of applicability for the latter (Sbragaglia et al., 2008). Latva-Kokko et al. showed the scaling of dynamic contact angles with regard to the capillary number and determined the slip length follows the classic Navier slipping wherein the velocity of the flow at the wall is proportional to the viscous stress at the wall. This slip length is proportional to the viscous length scale associated with spurious flow induced by the three-phase singularity (Latva-Kokko and Rothman, 2007).

1.2. Non-equilibrium effects

The studies discussed above are evaluated at equilibrium and thus do not give any insight into the dynamic quantities and their impact on multiphase flow through porous media. By equilibrium we mean that the liquid velocities are zero and the interface between the phases is stable. In 1987 Weitz et al. studied the dependence of velocity and capillary pressure and their impact on viscous fingering and determined the dynamic component of capillary pressure to have a stabilizing effect on the formation of viscous fingers (Weitz et al., 1987). Cueto-Felgueroso and Juanes employed a continuum model based upon thin film flow models to capture the effect of surface tension without introducing new independent parameters and found good agreement with experimental results. This work also confirmed the phenomenon wherein finger velocity and width increase with higher liquid infiltration velocity (Cueto-Felgueroso and Juanes, 2008). In 2012 Hilpert developed a model based upon the generalized Green-Ampt approach and showed its ability to correctly estimate the capillary pressure overshoot depending upon upstream and downstream liquid content as well as solid grain size. This formulation of capillary pressure is velocity-dependent as well as dependent upon liquid content (Hilpert, 2012). In 2011 Løvoll et al. performed experiments on liquid primary drainage and were able to generate collapsed curves relating the capillary number of a system and its corresponding pressure–saturation curve. They also postulated that the dynamic effects in the capillary pressure may be a combination of the viscous effects from the wetting phase in conjunction with the capillary pressure along the direction of the gaseous phase front (Løvoll et al., 2011). Work by Joekar-Niasar et al. has focused on employing pore network modeling with the addition of a dynamic capillary term to more accurately solve two-phase flow in a porous medium (Joekar-Niasar et al., 2010; Joekar-Niasar and Hassanizadeh, 2011; Joekar-Niasar and Hassanizadeh, 2012). Also reported are many results from experimental determinations of coefficient values for the strength of dynamic contributions to capillary pressure as determined by other researchers. They investigated the non-equilibrium capillary effects under drainage and imbibition as a function of saturation, viscosity ratio, and effective viscosity. Manthey et al. proposes an additional nondimensional number, the Dynamic number, to aid in relating the dynamic capillary to viscous forces as well as gravity. Values are characterized as a function of characteristic length and flow velocity, with front width found to be the best length scale (Manthey et al., 2008).

1.3. Aim of current work

In previous work we have examined the impact of microstructure on infiltration dynamics, particularly the relationship between particle sizes and porous layer thickness in combination with variable hydraulic pressures applied to the porous surface (Pettersson et al., 2020). It was determined that the particle packing influences the infiltration rate and homogeneity as determined by resultant pore size distribution and interfacial area. This work constitutes a complementary analysis of the microstructure influence on capillary pressure, resultant flow velocity, and a measure of the capillary number. In particular we show the effect of packing thickness on capillary behavior, ranging from cases where capillary suction forces dominate the infiltration dynamics to those wherein the capillarity opposes the primary flow gradient. We also observe an increased likelihood of the occurrence of fingering, which follows through the resultant competition between gravitational and capillary forces at the pore-scale. A predictive relationship is described for dynamic capillary pressure and flow velocity, based on the porous microstructure, which may be applied to aid in the design of substrates with regard to packing, flow velocity and green roof detention. A comparison is also drawn to the previously reported behavior of the dynamic component of capillary pressure.

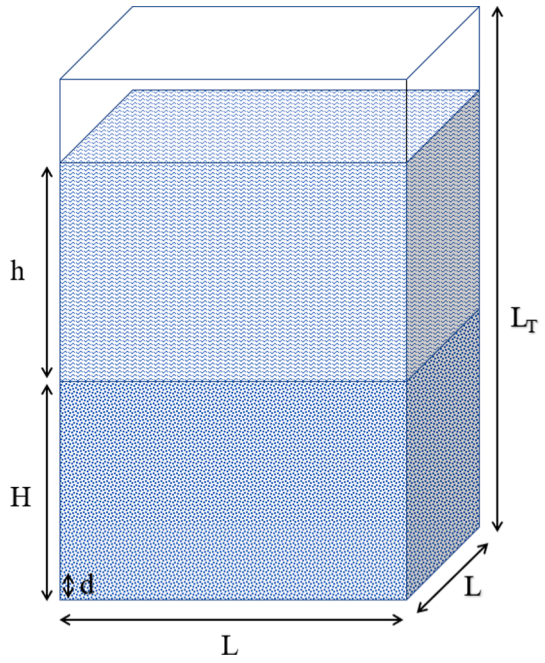

Fig. 1. Geometry representation with relevant measures, not to scale. L - lateral domain length, L_T - stream-wise domain total length, H - porous domain height, h - wetting phase layer height, d - particle diameter. Gravity acts in the downward vertical direction.

Table 1
Dimensionless quantities for each case, grouped by ϕ.

Case #	ϕ	h^*	Ca_c
1	10.1	10	0.041
2	10.1	13	0.025
3	10.1	15	0.041
4	6.7	6.7	0.092
5	6.7	10	0.092
6	6.7	11.3	0.074
7	5.1	5	0.167
8	5.1	7.5	0.167
9	5.1	15	0.167

2. Materials and methods

2.1. Simulation characterization parameters

Several simulations are constructed and run to reflect differing conditions of rainfall intensity and soil design, resulting in nine distinct domain configurations. Each domain consists of a porous subdomain and a void subdomain wherein the porous section acts as an analogue for a thin layer of soil with height H and the void domain allows for the initialization of the rain water as the wetting phase. Fig. 1 shows all of the relevant domain measurements that are introduced below.

2.1.1. Geometry and flow parameters

The porous subdomain is constructed as a randomly packed bed of monodisperse spherical particles with variable particle diameter d. The random packing was performed using the software Blender, which has been shown to be an effective method of generating such a packing, as by Boccardo et al. (2015). Five distinct porous layers are generated by modifying the particle diameter and porous subdomain height H while maintaining adherence to the particle size-minimum domain dimension requirement for a representative volume as defined in (Galindo-Torres et al., 2016). The particle sizes were chosen to reflect the properties of lightweight expanded clay aggregate (LECA). In addition to the porous subdomain height, the domain length perpendicular to the primary flow direction is given as L an is chosen such that the restriction for wall impact on the flow field is satisfied. The wetting phase is generated within the void subdomain as a layer of thickness h that lies directly above the porous subdomain. This is to reflect the hydrostatic pressure applied appropriate to surface water under extreme rainfall conditions in Gothenburg, Sweden as calculated directly from meteorological data from SMHI (Pettersson et al., 2020). The simulations are run with periodic boundary conditions in the primary flow direction and symmetric conditions in the lateral directions. It is worth to note that the setup is run as a falling head simulation, such that the water height decreases in time, rather than a constant head or pressure/flux condition. This is to prevent any artificial forcing from a pressure condition or from a fixed flux condition, which we can not know the magnitude of *a priori*. We consider a two-phase water-vapour system whose physical properties are the wetting and non-wetting phase density (ρ_w, ρ_{nw}) and dynamic viscosity (μ_{nw}, μ_w). In addition, we define the constant values for gravity g and surface tension γ. The simulated system is characterized by a density ratio and dynamic viscosity ratio of 35. The value of the density ratio is limited compared to real applications, so that we must consider that inertial effects are underestimated in our computations. However, we can correctly represent a two-phase system with the viscosity ratio close to real applications, and thus accurately take into account the viscous effects that are dominant in low-velocity flows in porous media (with capillary numbers much smaller than one), as the ones encountered during rain infiltration in green roof substrates.

2.1.2. Dimensionless parameters

In order to characterize the studied system, three characteristic dimensionless quantities are chosen. A dimensionless packing ratio $\phi = H/d$ is defined and acts as a measure of the thickness of particle layering within the porous subdomain. This parameter is used to categorize the effect of the packing, particularly as it effects not only the mean pore size but also the local porosity along the packing direction. Amore thorough discussion may be found in (Pettersson et al., 2020). Another parameter representing the dimensionless wetting phase height is given as $h^* = h/d$. This parameter represents a measure of the approximate pore sizes in the microstructure against the applied hydrostatic pressure from the surface. We assume the particle size to be of the same magnitude as pore size for a randomly packed bed, as determined in previous work (Pettersson et al., 2020). The final characteristic quantity is the pore-scale characteristic capillary number,

$$Ca_c = \frac{u_c \mu_w}{\gamma}, \tag{2}$$

$$u_c = \frac{\rho_w g d^2}{\mu_w}, \tag{3}$$

where u_c is the pore-scale characteristic velocity. The pore-scale capillary number represents the importance of gravity-induced viscous forces over surface tension at the pore scale. The values for each of the dimensionless parameters is given in Table 1.

It is important to mention that prior to running the multiphase simulations a study was undertaken to determine appropriate lattice resolution, as a failure in this regard will lead to erroneous results. The lattice resolution used in this work is the result of a grid convergence test, the details of which can be found in (Pettersson et al., 2020).

2.2. Lattice Boltzmann method

The numerical method employed in this work is identical to that which is used in our previous works (Pettersson et al., 2020; Farzaneh et al., 2021), therefore we will not provide all information in full detail, but rather give a brief overview of the methodology used.

The lattice Boltzmann method solves the Boltzmann particle trans-

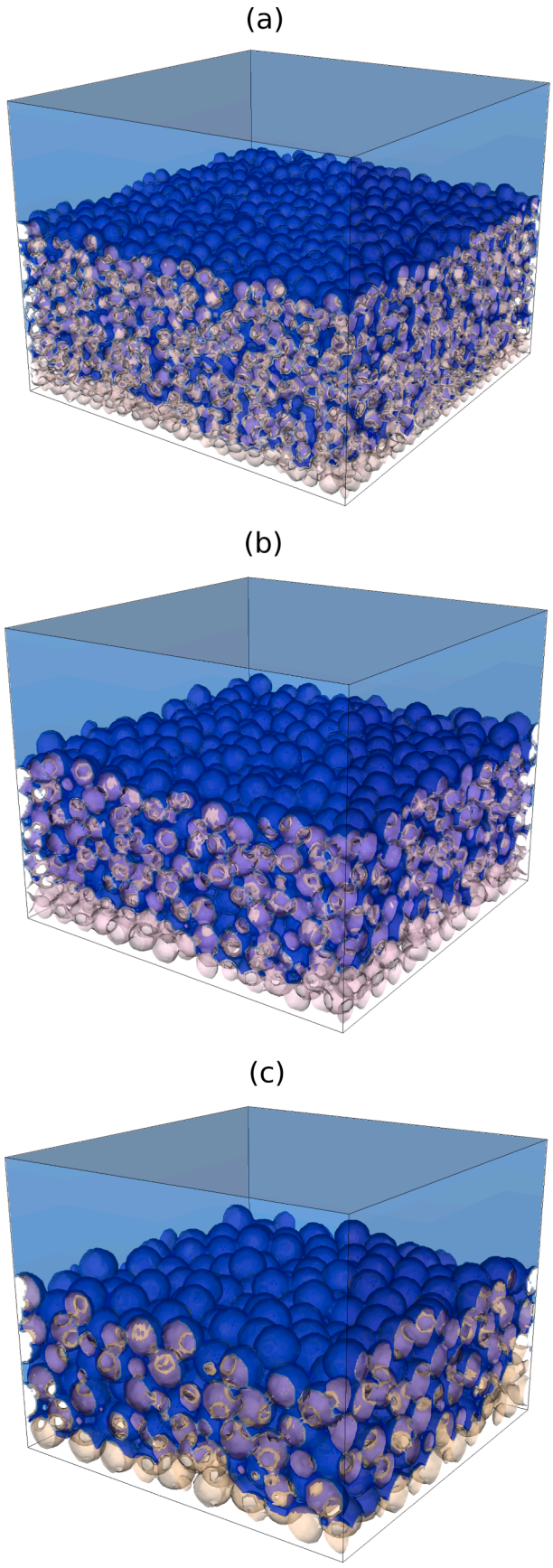

Fig. 2. Infiltration patterns at timestep t = 250,000 for (a) $\phi = 10.1, h^* = 15$, (b) $\phi = 6.7, h^* = 10$, (c) $\phi = 5.1, h^* = 7.5$.

port equation, which includes motion through streaming as well as collisions. It is an ideal choice for solving flows in porous media due to the complex geometry involved and allows for detailed information of the flow dynamics to be extracted at the pore scale. The system is solved on a lattice structure wherein each lattice element consists of a centroid and nodes placed on a cubic convex hull. Small-scale mass and momentum are distributed along the lattice nodes governed by probabilities appropriate for the chosen lattice geometry such that the macroscopic properties of the fluid are preserved (Succi, 2001). A 3D regular cubic lattice with 19 degrees of freedom for movement (D3Q19) is used and the solved equation is of the form

$$f_r(\boldsymbol{x}+\boldsymbol{c}_r\delta t, t+\delta t) - f_r(\boldsymbol{x},t) = -\tau^{-1}\left(f_r(\boldsymbol{x},t) - f_r^{eq}(\boldsymbol{x},t)\right) + F_r \tag{4}$$

where $f_r(\boldsymbol{x},t)$ is the distribution function at position $\boldsymbol{x}$ and time t along the r-th direction; $\boldsymbol{c}_r$ is the so-called discrete velocity vector along the r-th direction over time interval δt; f_r^{eq} is the equilibrium distribution function; and τ is the mean collision time and is related to kinematic viscosity by $\nu = c_s^2(\tau - 0.5\delta t)$. A body force F_r as formulated by Guo (Guo et al., 2002) is applied to the fluid, which mimics the effect of gravity, and is given by

$$F_r = \left(1 - \frac{1}{2\tau}\right) w_r \left(\frac{\boldsymbol{c}_r - \boldsymbol{u}}{c_s^2} + \frac{\boldsymbol{c}_r \cdot \boldsymbol{u}}{c_s^4}\boldsymbol{c}_r\right)\left(\rho \boldsymbol{g}\right) \tag{5}$$

with $\boldsymbol{g}$ representing gravitational acceleration, $\boldsymbol{u}$ the fluid velocity, w_r is the weighting parameter; ρ is the density; c_s is the speed of sound; and $\boldsymbol{u}_{eq}$ is the Chen equilibrium velocity (Chen et al., 2014); calculated as

$$\boldsymbol{u}_{eq} = \rho \boldsymbol{u} + (\tau - 1/2) F_{sc}. \tag{6}$$

The Shan-Chen fluid interaction formulation (Shan and Chen, 1993) is used to model the surface tension using an inter-particle force that can act via attraction or repulsion of particles in the collision operator, in addition to elastic collisions. A pseudo-potential function $\Psi(\rho)$ determines the interaction strength between the phases, and in combination with the the Shan-Chen force, closes the system with the resultant non-ideal equation of state. This equation of state describes the thermodynamic equilibrium between the phases. Respective of order of introduction, these equations are

$$F_{sc} = -G\Psi\left(\mathbf{x}, t\right) \sum_r w_r \Psi\left(\boldsymbol{x} + \boldsymbol{c}_r \delta t, t\right) \boldsymbol{c}_r, \tag{7}$$

$$\Psi(\rho) = 1 - e^{-\rho}, \tag{8}$$

$$p = \rho c_s^2 + \frac{G}{2} c_s^2 \Psi^2, \tag{9}$$

where $G = -5.5$ is the interaction strength between the phases. Attraction occurs when G is negative and vice versa. The recovered macroscopic quantities density and velocity, $(\rho, \boldsymbol{u})$ are related to the previously defined hydrodynamic moments by:

$$\rho = \sum_r f_r, \tag{10}$$

$$\rho \boldsymbol{u} = \sum_r \boldsymbol{c}_r f_r + 1 \Big/ 2\ \rho \boldsymbol{g} + 1 \Big/ 2\ F_{sc}, \tag{11}$$

A moving wetting-nonwetting phase contact line characterized by a contact angle chosen under equilibrium conditions is used to determine the interaction between the solid and wetting phases. This contact angle is determined by Young's equation and is calculated using spatial averaging of the pseudo-potential function. The De Maio et al. (2011) formulation for the force at the solid wall (Ψ_{wall}) is of the form:

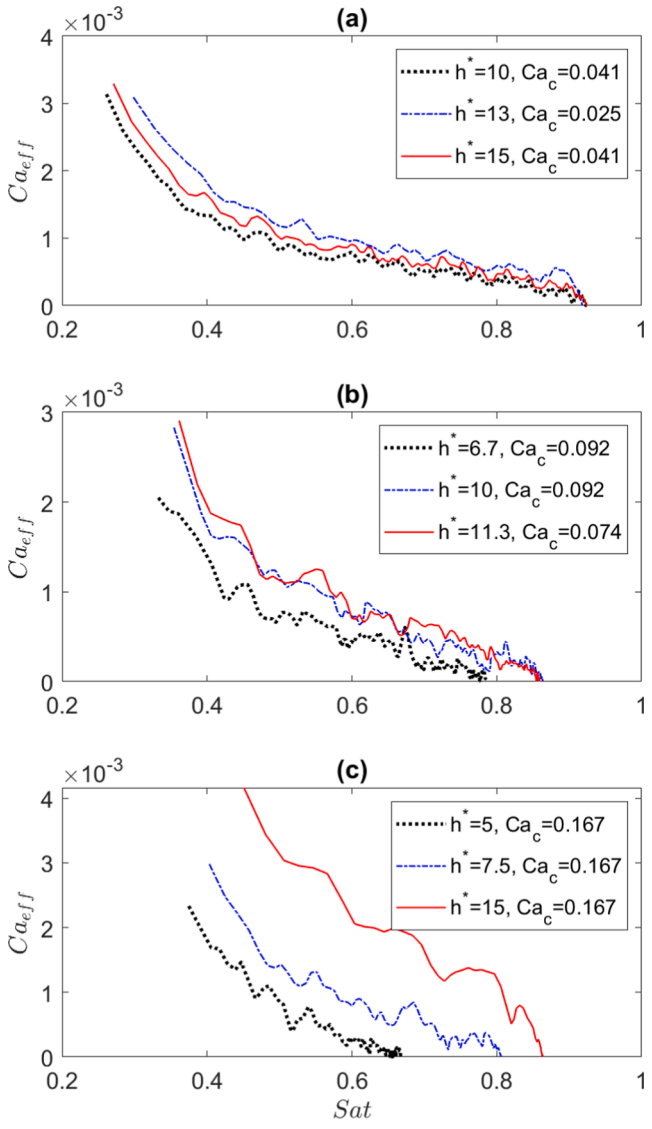

Fig. 3. (a) Effective capillary number Ca_{eff} as a function of saturation, $\phi = 10.1$. (b) $\phi = 6.7$ (c) $\phi = 5.1$. Approximately $Ca_{eff} \propto 1/Sat$ after initial infiltration stage.

$$\Psi_{wall} = \Psi\left(N^{-1}\sum_{N}\rho + \Delta_w\right) \tag{12}$$

where Ψ is the density-dependent function and N the nearest fluid computational nodes. Δ_w represents a "surplus density" which can be tuned to exhibit the behavior of different contact angles. The method requires enforcement of a constant density gradient at the walls and additional information regarding Δ_w and the contact angle can be found in Benzi et al. (2006). In this work the equilibrium contact angle is fixed at $\Delta w = 0.02$ corresponding to $\theta = 82°$, which represents a slightly hydrophilic material, found in materials used in green roofs, such as LECA. It is also noteworthy that the lattice Boltzmann method has an equilibrium contact angle (no applied force) however, in the presence of other mechanical forces acting on the interface this angle can change slightly.

3. Results and discussion

We wish to examine the infiltration patterns qualitatively for each particle value of ϕ approximately halfway through the simulation run-

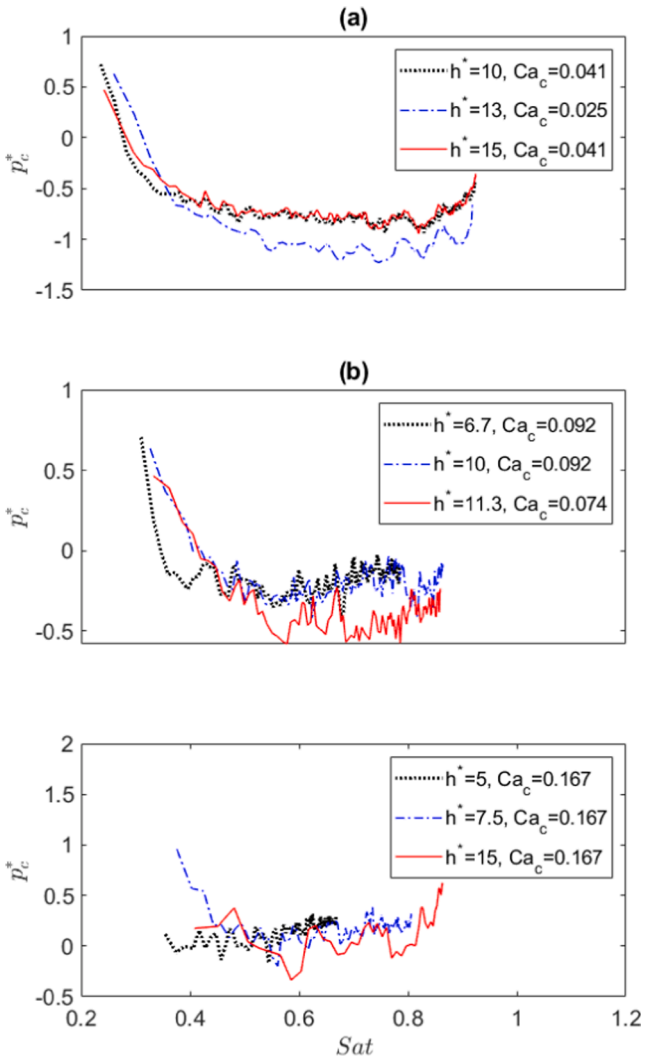

Fig. 4. Mean capillary pressure $p_c^*(Sat)$ as a function of saturation: (a) $\phi = 10.1$. (b) $\phi = 6.7$ (c) $\phi = 5.1$. $p_c^* > 0$ represent capillary forces acting against the flow gradient; $p_c^* < 0$ represents capillary suction.

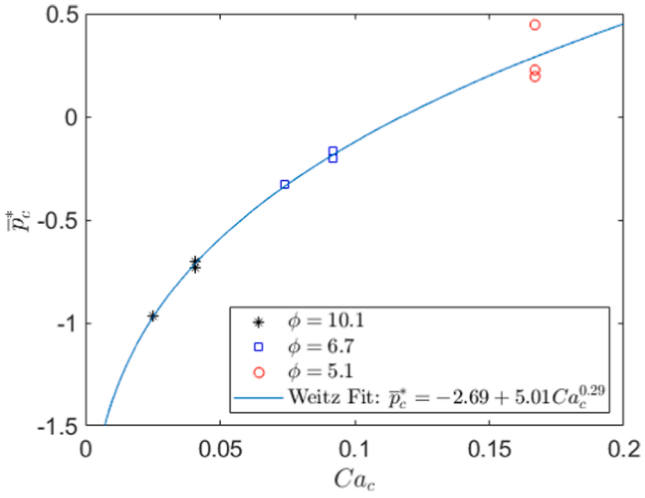

Fig. 5. Collapsed curve of mean p_c^* as a function of Ca_c. Weitz fit given by $\overline{p_c^*} = -2.687 + 5.014\overline{Ca_c}^{0.2912}$.

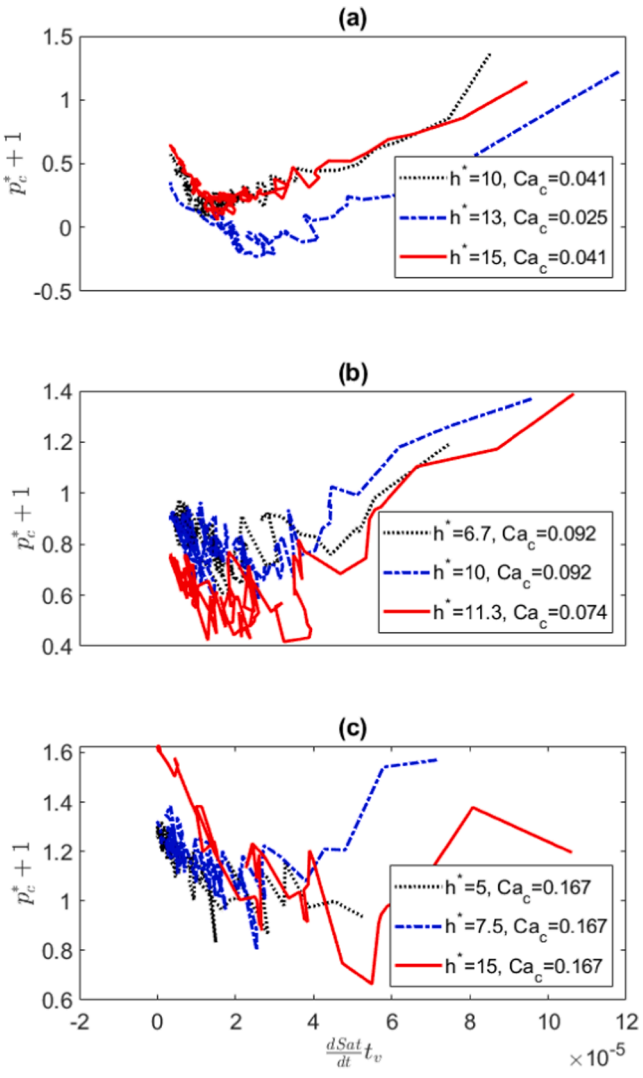

Fig. 6. Approximation of τ, high infiltration rate values correspond to simulation start.

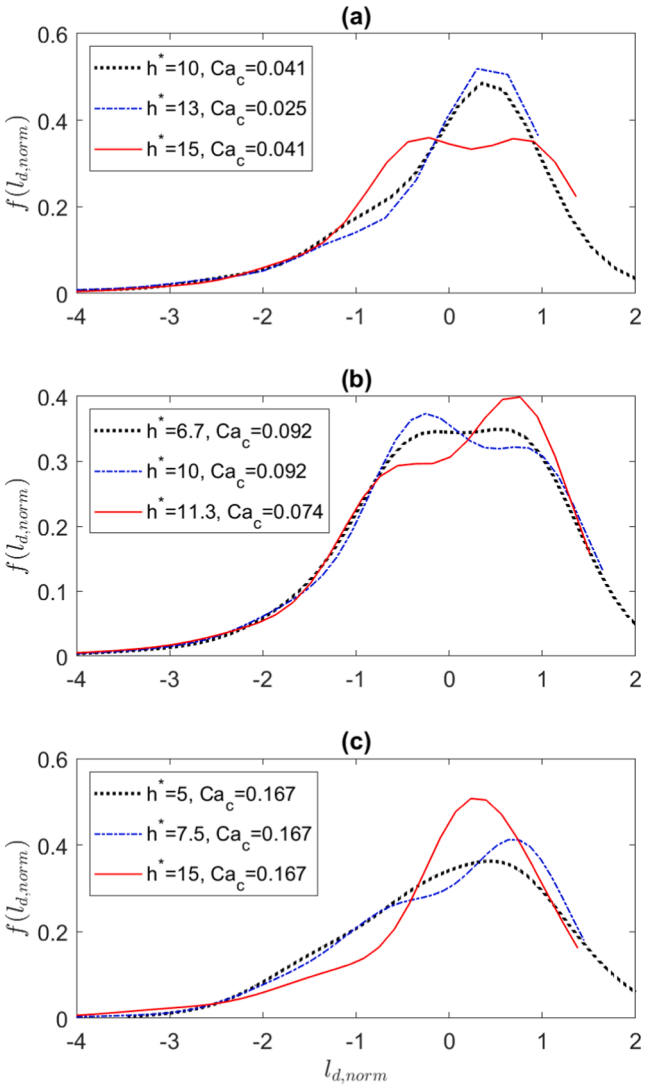

Fig. 7. PDFs ($f(l_{d,norm})$) of normalized wetting phase infiltration depth ($l_{d,norm}$) as given in standard errors from mean infiltration depth. Single high peaks near $l_{d,norm} = 0$ indicate highly homogeneous infiltration. (a) $\phi = 10.1$ (b) $\phi = 6.7$ (c) $\phi = 5.1$.

time, corresponding to the 250,000th timestep ($t^* = 172$). The results are plotted in Fig. 2. It appears that the infiltration has almost reached the bottom of the porous layer in all configurations however in (b) and (c) there seems to be less homogeneity of the wetting front. Certainly in (c) we can see on the right corner a zone where infiltration has stalled after the initial particle layers. This is consistent with the established notion that greater energy is required to advance the wetting front over the greater surface area, which causes more inhomogeneous infiltration patterns when subjected to identical conditions, as seen in our previous investigation (Pettersson et al., 2020).

In order to examine the interdependence of velocity and saturation (*Sat*) we introduce the effective capillary number Ca_{eff} which is calculated as

$$Ca_{eff} = \left(\frac{\mathrm{d}Sat}{\mathrm{d}t}H\right)\frac{\mu_w}{\gamma} = U\frac{\mu_w}{\gamma}, \tag{13}$$

where the velocity is given by the rate of overall stream-wise infiltration over time. Saturation is calculated by summing the total nodes occupied by the wetting phase and dividing by the total available void space within the porous domain subsection. In Fig. 3 we see an overall decrease in velocity as the saturation increases for all cases. This decrease of Ca_{eff} as a function of saturation remains almost constant after the initial phase of infiltration through the uppermost layer. This can attributed to our definition of the infiltrating velocity and the increasing viscous resistance to the infiltration fluid as saturation increases.

When the packing ratio is larger as in (a) and (b) we see little effect of the hydrostatic pressure h^* on infiltration velocity; however when the packing ratio is small as in (c), we observe a larger variation in the infiltration rate along with little distinction between the initial stage and subsequent infiltration rate. This observation suggests that when the packing ratio is small, the magnitude of the hydraulic pressure has a substantial effect on the flow dynamics, given also that dynamic effects and gravitational forces at the pore scales, (larger Ca_c), become important. This impact on the fluid velocity can be better understood when one examines the capillary pressure within the porous network.

In Fig. 4 we plot the dimensionless capillary pressure–saturation curves and see a correlation regarding ϕ and the corresponding capillary pressure, with lower values exhibiting hydrophobic characteristics. The capillary pressure using the method reported in Appendix A and is non-dimensionalized by dividing the pressure by the ratio of surface tension to particle size.

$$p_0 = \gamma/d, \tag{14}$$

$$p_c^* = (p_w - p_{nw})/p_0. \tag{15}$$

In Fig. 4 we observe a trend of the average values of the capillary pressure over differing values of ϕ and Ca_c, similar to that of the effective capillary number. In the case of large ϕ, (a), we clearly see that the applied hydrostatic pressure has almost no effect on the capillary pressure. The only notable difference between the cases pictured in (a) is the negative shift in the case with lower pore-scale velocity. The values of the capillary pressures are negative in all cases in (a) where Ca_c is low, indicating that capillary suction is occurring as a mechanism for pore infiltration. A similar effect can be seen when the packing ratio is reduced and the pore-scale velocity is thus increased. While in (b) we see much the same behavior it is worthwhile to point out that the average value of the capillary pressure is less negative than in the prior cases, indicating a weakening of the capillary suction contribution. It can also be seen that oscillations in the pressure with greater magnitude occur, which may be due to the greater forces required to overcome the surface tension resistance for invasion of the larger pores. This trend is continued in (c) where the capillary pressure is now positive on average, denoting a capillary action acting against the flow. The magnitudes of the oscillations are still present and indeed in this case the values of the capillary pressure are more similar, which clearly shows the role of the pore-scale velocity on determining the capillary pressure, rather than the hydrostatic pressure.

The cases with lower values of ϕ exhibit the behavior of a valve-like barrier on the flow as defined by positive values of capillary pressure. This positive capillary pressure has been found to appear in cases with higher injected fluid velocity as firstly described by Weitz et al. (1987). Weitz et al. showed that dynamic capillary pressure is dependent upon this injected fluid velocity. This effect has also been observed in cases where a non-wetting fluid is displacing a more dense wetting fluid under gravitational forces (Løvoll et al., 2011).

In the cases investigated herein a more dense fluid is invading a less dense one. In such a case we observe a similar general dynamic trend of the capillary pressure, whereby increasing the pore-scale gravitational effects (Ca_c), we notice an increase of the capillary pressure. We also observe a marked effect of the packing ratio, determining the porous microstructure. This observation tells us that it is possible to regulate the capillary pressure by modifying the particle packing as a means to regulate the flow behavior within the system.

In order to get a better idea of the interdependence of the velocity, capillary pressure, saturation, and microstructure we attempt to collapse all cases onto a single curve. Fig. 5 displays the time-averaged capillary pressure as a function of the characteristic capillary number. The average for the capillary pressure is calculated as shown:

$$\overline{p}_c^* = \frac{1}{(t_{end} - t_0^+)} \int_{t=0^+}^{t_{end}} p_c^*\left(t\right) \mathrm{d}t. \tag{16}$$

The time averaging neglects the first time instance wherein the infiltration rate constitute outlier values due to initialization of the infiltrating liquid. Thus $t = 0^+$ represents the second saved iteration and $t = t^{end}$ represents an iteration whereat the effective capillary number becomes smaller than a given threshold value that indicates negligible infiltration (here set at $Ca_{eff} < 10^{-4}$). In Fig. 5 the results have been plotted and are clustered by packing ratio. The points show an excellent correlation between the time-averaged capillary pressure and Ca_c across the threshold from negative to positive values of capillary pressure. A similar relationship is shown for instance in Weitz et al. however in that work the dynamic contribution to capillary pressure is related to velocity by the equation

$$p_c^* = \beta\left(-1 + KN_{Ca}^x\right), \tag{17}$$

$$N_{Ca} = \mu U/\gamma. \tag{18}$$

where $\beta = d/r_{th}$ is the ratio of particle diameter d to r_{th}, with r_{th} some characteristic pore throat radius. N_{Ca} is the capillary number and K, x are fitting parameters representing the strength of the dynamic contribution, dependent upon initial velocity. We choose to use the characteristic capillary number rather than the Weitz definition as they controlled the entry velocities whereas in our case the medium velocities are determined by the competition between gravitational and surface tension forces acting at the pore scale. Thus, the dynamic contribution to capillary forces, formulated though Ca_c, is expected to depend on the pore size, as predicted by Eqs. 2 and 3, with larger pores inducing a larger dynamic effect on the pore-scale pressure distribution. Despite the differences in the investigated physical system we see a striking similarity in the results when we apply a least squares fit of our collapsed data points to the modified equation of Weitz et al., as shown in Fig. 5. It is worth pointing out as well that the results reported in their work were taken at equilibrium conditions whereas in our work we use a time-averaged capillary pressure, but the relationship still holds. The cases with the highest ϕ value exhibit a lower capillary pressure and the values scale directly as we decrease ϕ. They range from capillary suction dominated to more neutral in terms of the driving force for infiltration. The clustering remains similar for $\phi = 10.1$ and $\phi = 6.7$ however the capillary pressure is shifted more in the positive direction, denoting decreasing influence of capillary suction driven infiltration. Weitz reported values of $\beta \approx -4.1 \pm 0.4$ whereas in our worth the value is -2.7 which is very similar. The same holds true for $K \approx 30 \pm 5$ versus 5 in this work and finally $x \approx 0.5 \pm 0.1$. This close agreement shows the physical consistency of our results with experimental work as well as a method by which the capillary forces can be predicted as a function of the characteristic capillary number. It should also be noted here that capillary pressure is determined by the characteristic capillary number and not on the hydrostatic effects, represented by h^*. Ultimately, by modifying the packing ratio we can alter the capillary pressure by way of increasing the pore sizes, resultant by choosing larger particles. This observation can be invaluable from a design perspective to aid in understanding the behavior of capillary pressure of different substrates under a variety of chosen conditions, prior to extensive testing.

3.1. Modeling infiltration with dynamic capillary pressure

We make use of the Washburn equation (Washburn, 1921) to aid in elucidating the link between the behavior of the effective capillary number, the capillary pressure, and the Weitz fit as shown in Fig. 5. We can thus formulate the following proportionality:

$$\frac{\mathrm{d}Sat}{\mathbf{d}t} H \propto \frac{d^2}{\mu_w} \frac{1}{SatH}\left[\rho_w g\left(h - SatH\right) - p_c\right], \tag{19}$$

where the first term within brackets on the right hand side represents the contribution of gravity-induced forces and the second term on the right hand side the capillary action. This proportionality is consistent with the well-known Washburn relation of infiltration length (in our case saturation) proportional to the square root of time if the gravitational component is neglected and the capillary pressure is constant as in the classical definition. As a result of this formulation we express the effective capillary number introduced earlier in a similar manner:

$$Ca_{eff} \propto Ca_c\left(\frac{h^* - Sat\phi}{Sat\phi}\right) - \frac{p_c^*}{Sat\phi}. \tag{20}$$

We see an inverse relationship between the effective capillary number and saturation occurs when either the gravity-induced forces are absent ($Ca_c = 0$) or the infiltration is low (low value of Sat). This relationship can be seen in Fig. 3 as we have a sufficiently low infiltration for this proportionality to occur. This also explains why we see faster infiltration in the beginning of the simulations, particularly as the packing ratio is decreased in magnitude. In addition, as saturation increases we expect to see a decrease in effective capillary number, which again is visible in Fig. 3 in all cases. From Eq. 20, we also see that when

the value of the packing ratio ϕ is low (large pores compared to medium thickness), the contribution of the first term on the right hand side of Eq. 20 to the infiltration dynamics, i.e. the gravitational term, is increased. However, as our analysis on the effective capillary pressure reveals (see Fig. 5), low packing ratios likely trigger positive values of capillary pressures, which in turn counteract the gravitational contribution. In other words, low packing ratios and large particles induces significant gravitational forces (high Ca_c), which determine a faster initial infiltration rapidly slowed down by a dynamic capillary force acting adversely to the flow.

3.2. Comparison of dynamic capillary contribution

In order to compare these results concerning the behavior of the dynamic capillary pressure we compare our results to that of other researchers. Several such models can be found in Manthey et al. (2005) and results of many efforts have been reported in (Joekar-Niasar and Hassanizadeh, 2011). The comparison can be done by way of plotting the changes in saturation against the capillary pressure as given by

$$p_c^* + 1 \approx \epsilon \frac{\tau}{p_0} \frac{\mathrm{dSat}}{\mathrm{dt}} \tag{21}$$

In Fig. 6 we plot the change in saturation (infiltration rate) against the capillary pressure. The results give an approximation of the dynamic capillary pressure coefficient τ. The infiltration rate is non-dimensionalized using the characteristic viscous time $t_v = d^2/\nu_w$. We can see clearly we have a quasi-linear dependence, indicative of a constant value for *tau* for high values of infiltration. It is clear however that the model does not work for low infiltration rates and low values of ϕ, where this quasi-linear dependence is lost.

3.3. Infiltration homoegeneity

In Fig. 7 we plot the probability distribution functions (PDFs) of infiltration depth at timestep $t_{lb} = 250,000$ and examine the resultant distributions. In these cases homogeneous infiltration is characterized by a singular spike near 0 whereas less homogeneous flow is shown by bimodal behavior as well as less extreme slopes. In (a) we see two of the three cases exhibit a tighter distribution around the mean infiltration depth, denoting a more homogeneous wetting front; however the case with higher hydraulic pressure exhibits less homogeneity. In both (b) and (c) we see similarly less homogeneous infiltration patterns with the exception of the case where $h^* = 15, Ca_c = 0.167$ where once again the infiltration appears more homogeneous. This aberration in the results can be explained by the quick convergence of this case to an equilibrium state due to the high hydraulic pressure applied. The general observed trend suggests that when increasing the hydraulic pressure and reducing the packing ratio; while the flow exhibits higher infiltration rates, the suction mechanism (hydrophilicity) is inhibited and an adverse capillary pressure arises. This pressure induces less homogeneous infiltration patterns. In observing this trend of less homogeneous flow for lower ϕ values, we have shown that by applying an initial hydrostatic pressure above a certain threshold to the system we can increase the dynamic capillary pressure (as defined in this work) and generate the conditions under which the porous medium acts in a hydrophobic manner, slowing the resultant wetting phase velocity within the pores. This lower velocity generates higher occurrences of fingering, which is consistent with the works of Weitz et al. (1987) and Cueto-Felgueroso and Juanes (2008). Thus by choosing a particular packing ratio one can effectively determine the infiltration rate of the system by bringing about the conditions wherein an inherently hydrophilic or borderline material can act in a hydrophobic manner.

This particular property can be of use in designing green roof soil substrates where a particle size can be chosen with a specific hydraulic load to behave in a hydrophobic manner and slow pore infiltration. By layering differently sized particle one can create a system that acts differently under different hydraulic loads without resorting to overly-thick individual layers. This can reduce material use and weight applied to the structure, depending on the material chosen.

4. Conclusion

This work provides an analysis of the impact of the porous microstructure on infiltration dynamics of thin porous media by establishing the relationships between saturation, dynamic capillary pressure, effective capillary number, and characteristic capillary number. The infiltration rate of media with a larger packing ratio is largely unaffected by the magnitude of hydraulic pressure whereas in for lower values of the packing ratio the hydraulic pressure plays a more significant role. This is due to the fact that dynamic effects and gravitational forces at the pore scales, (larger Ca_c), become important. An inverse relationship between the effective capillary number and saturation occurs when either the gravity-induced forces are absent or the infiltration is low as is seen in this work. We see that the capillary pressure depends only upon Ca_c and as the packing ratio decreases capillary suction is no longer the dominant driver of infiltration and in the most extreme cases the capillarity acts against the infiltration gradient in a valve-like manner.

The relationship between the characteristic capillary number and time-averaged capillary pressure is collapsed onto a singular plot and fit to an empirical function derived from experimental work. This model allows us to represent the effects of the microstructure and the resulting infiltration rate on the capillary pressure present within the medium. By combining the classic Washburn solution for infiltration with the power-law scaling of the capillary pressure we show that is possible to predict the infiltration within different substrates' microstructures under different rain intensity events. This can be invaluable from a design perspective to understand the behavior of capillary pressure of different substrates under a variety of chosen flow rates prior to extensive testing.

A comparison is made to the works of other researches with regard to the contribution of the dynamic component of the capillary pressure, with good agreement observed, indicating the validity of the method proposed in this work to capture this effect accurately. In addition, flow homogeneity is dependent upon the capillary pressure, which when acting against the infiltrating wetting phase, contributes to fingering of the flow within the porous matrix.

While the results in this work are consistent with the findings of other researchers, it should be noted that several assumptions have been made in the work; the fixed equilibrium contact angle, the lack of any thermal contribution, the use idealized packed spherical beds, and the omission of drainage within the work. These aspects should be addressed in order for future works to approach a more realistic case and thus represent opportunities for future investigation.

CRediT authorship contribution statement

Kaj Pettersson: Software, Validation, Formal analysis, Investigation, Writing - original draft, Writing - review & editing. **Dario Maggiolo:** Conceptualization, Methodology, Software, Validation, Investigation, Writing - review & editing, Supervision, Project administration, Funding acquisition. **Srdjan Sasic:** Conceptualization, Resources, Writing - review & editing, Supervision, Project administration, Funding acquisition. **Pär Johansson:** Writing - review & editing, Supervision. **Angela Sasic Kalagasidis:** Conceptualization, Writing - review & editing.

Declaration of Competing Interest

The authors declare that they have no known competing financial interests or personal relationships that could have appeared to influence the work reported in this paper.

Acknowledgements

This work was supported by the Swedish Research Council for Environment, Agricultural Sciences and Spatial Planning (FORMAS), Grant Nos. 2015–00173 and 2019–01261. The computations were enabled by resources provided by the Swedish National Infrastructure for Computing (SNIC) at HPC2N partially funded by the Swedish Research Council through grant agreement No. 2018–05973.

Appendix A

The capillary pressure is calculated for every time step in the manner described here. Each interface within the medium is determined and the pressure on each side is calculated as an average value within a specified number of nodes of the interface. Due to the diffuse nature of the interface of this lattice Boltzmann approach, a threshold value is chosen to determine which nodes are assigned as the liquid and wetting phase. All of the calculated capillary pressures at all interfaces are stored for each iteration along with their locations and a statistical analysis is undertaken for each timestep, resulting in a mean and standard error value for the capillary pressure. In Fig. 8 an example interface is shown and the density profile across it is plotted. An examination of the standard errors of the capillary pressures at each timestep was undertaken and were neglected from Fig. 4 on the basis of their magnitude in order to improve figure clarity.

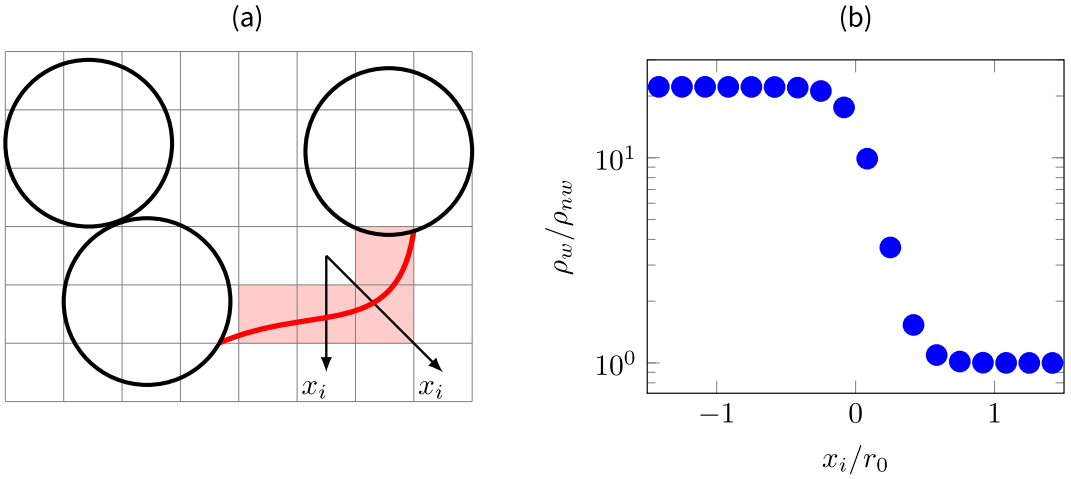

Fig. 8. (a) Sketch representing the two-phase interface (red line) identified on the lattice Boltzmann grid. The capillary pressure is calculated along directions x_i normal to the interface. (b) An example of density profile at the two-phase interface along x_i. The pressures at each phase are calculated at a distance $r_0 = 6$ lattice points from the interface ($x_i = 0$).

Appendix B

A quantification of the dynamic component of the capillary pressure in terms of a coefficient that other researches have used to isolate this contribution is attempted. While a direct comparison is difficult as our cases are run fully in a dynamic environment and thus an equilibrium capillary pressure is not calculable; we have opted to approximate this coefficient as defined by Kalaydjian (1987) whose model is strictly only valid for cylindrical pores. The formulation is given as

$$p_c + \frac{2}{R}\gamma = \tau_K \epsilon \frac{\partial \mathrm{Sat}}{\partial \mathrm{t}}, \tag{22}$$

where R is the pore throat radius and τ_K is the fitting parameter representing the strength of the dynamic contribution. We note here that a range of values for R were tested. By calculating the left hand side as the capillary pressure we plot the evolution of τ_K as a function of saturation in Fig. 9. If one compares to results reported in Joekar-Niasar and Hassanizadeh (2011), with $M \ll 1$ and $\frac{\partial \tau_K}{\partial Sat} > 0$. We capture the dynamic capillary pressure contribution to the flow and how it increases as higher levels of saturation are reached. While other researchers have reported the value of τ to be exclusively positive, we see here that its value is negative in several cases wherein $R = 5$ is taken as an average pore throat, though a range of values were tested. It is very important to stress here that the mathematical models using the damping term require that $\tau_K \geqslant 0$ for the existence of a solution, as outlined in (Mikelic, 2010; Koch et al., 2013; and Cao and Pop, 2016). Some of our results do not conform with this restriction as we have here provided only a single rough estimate of the equilibrium capillary pressure. Indeed, if we reduce the average pore throat radius we eliminate any negative values for τ_K. Rather than focus solely on the value of τ_K we would stress more its evolution in time, which appears to be quasi-linear, particularly at lower values of saturation, which again matches results reported by others though its value oscillates wildly when higher saturation values are reached.

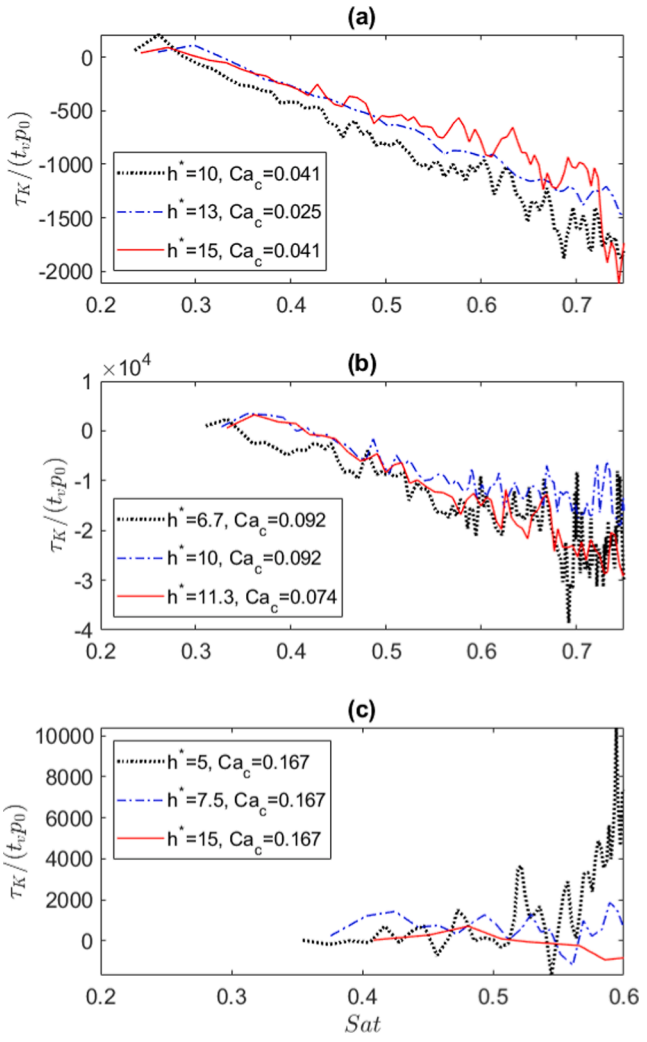

Fig. 9. τ_K(Sat): (a) $\phi = 10.1$ (b) $\phi = 6.7$ (c) $\phi = 5.1$.

References

Akhlaghi Amiri, H., Hamouda, A., 2014. Pore-scale modeling of non-isothermal two phase flow in 2d porous media: Influences of viscosity, capillarity, wettability and heterogeneity. Int. J. Multiph. Flow 61, 14–27. https://doi.org/10.1016/j.ijmultiphaseflow.2014.01.001.

Athukorallage, B., Iyer, R., 2016. Investigation of energy dissipation due to contact angle hysteresis in capillary effect, Vol. 727, doi:10.1088/1742-6596/727/1/012003.

Benzi, R., Biferale, L., Sbragaglia, M., Succi, S., Toschi, F., 2006. Mesoscopic modeling of a two-phase flow in the presence of boundaries: The contact angle, Physical Review E - Statistical, Nonlinear, and Soft Matter Physics 74 (2). doi:10.1103/PhysRevE.74.021509.

Bliss, D., Neufeld, R., Ries, R., 2009. Storm water runoff mitigation using a green roof. Environ. Eng. Sci. 26 (2), 407–418. https://doi.org/10.1089/ees.2007.0186.

Boccardo, G., Augier, F., Haroun, Y., Ferré, D., Marchisio, D., 2015. Validation of a novel open-source work-flow for the simulation of packed-bed reactors. Chem. Eng. J. 279, 809–820. https://doi.org/10.1016/j.cej.2015.05.032.

Brooks, R.H., Corey, A., 1964. Hydraulic properties of porous media. In: Hydrology Papers, no. 3. Colorado State University.

Cao, X., Pop, I., 2016. Degenerate two-phase porous media flow model with dynamic capillarity. J. Diff. Eqs. 260 (3), 2418–2456. https://doi.org/10.1016/j.jde.2015.10.008.

Chen, L., Kang, Q., Mu, Y., He, Y.-L., Tao, W.-Q., 2014. A critical review of the pseudopotential multiphase lattice boltzmann model: Methods and applications. Int. J. Heat Mass Transf. 76, 210–236. https://doi.org/10.1016/j.ijheatmasstransfer.2014.04.032.

Cueto-Felgueroso, L., Juanes, R., 2008. Nonlocal interface dynamics and pattern formation in gravity-driven unsaturated flow through porous media, Physical Review Letters 101 (24). doi:10.1103/PhysRevLett.101.244504.

De Maio, A., Palpacelli, S., Succi, S., 2011. A new boundary condition for three-dimensional lattice boltzmann simulations of capillary filling in rough micro-channels. Commun. Comput. Phys. 9 (5), 1284–1292. https://doi.org/10.4208/cicp.141009.241110s.

Farzaneh, M., Ström, H., Zanini, F., Carmignato, S., Sasic, S., Maggiolo, D., 2021. Pore-scale transport and two-phase fluid structures in fibrous porous layers: Application to fuel cells and beyond. Transp. Porous Media 136 (1), 245–270. https://doi.org/10.1007/s11242-020-01509-7.

Ferrari, A., Jimenez-Martinez, J., Borgne, T., Méheust, Y., Lunati, I., 2015. Challenges in modeling unstable two-phase flow experiments in porous micromodels. Water Resour. Res. 51 (3), 1381–1400. https://doi.org/10.1002/2014WR016384.

Galindo-Torres, S., Scheuermann, A., Li, L., 2016. Boundary effects on the Soil Water Characteristic Curves obtained from lattice Boltzmann simulations. Comput. Geotech. 71, 136–146. https://doi.org/10.1016/j.compgeo.2015.09.008.

Gallage, C., Kodikara, J., Uchimura, T., 2013. Laboratory measurement of hydraulic conductivity functions of two unsaturated sandy soils during drying and wetting processes. Soils Found. 53 (3), 417–430. https://doi.org/10.1016/j.sandf.2013.04.004.

Gostick, J., Aghighi, M., Hinebaugh, J., Tranter, T., Hoeh, M., Day, H., Spellacy, B., Sharqawy, M., Bazylak, A., Burns, A., Lehnert, W., Putz, A., 2016. Openpnm: A pore network modeling package. Computing Sci. Eng. 18 (4), 60–74. https://doi.org/10.1109/MCSE.2016.49.

Hilpert, M., 2012. Velocity-dependent capillary pressure in theory for variably-saturated liquid infiltration into porous media, Geophysical Research Letters 39 (6). doi:10.1029/2012GL051114.

Janetti, E., Riva, M., Guadagnini, A., 2017. Effects of pore-scale geometry and wettability on two-phase relative permeabilities within elementary cells, Water 9 (4). doi:10.3390/w9040252.

Guo, Z., Zheng, C., Shi, B., 2002. Discrete lattice effects on the forcing term in the lattice boltzmann method. Phys. Rev. E 65. https://doi.org/10.1103/PhysRevE.65.046308.

Joekar-Niasar, V., Hassanizadeh, S.M., 2011. Effect of fluids properties on non-equilibrium capillarity effects: Dynamic pore-network modeling. Int. J. Multiph. Flow 37 (2), 198–214. https://doi.org/10.1016/j.ijmultiphaseflow.2010.09.007.

Joekar-Niasar, V., Hassanizadeh, S.M., 2012. Analysis of fundamentals of two-phase flow in porous media using dynamic pore-network models: A review. Critical Rev. Environ. Sci. Technol. 42 (18), 1895–1976. https://doi.org/10.1080/10643389.2011.574101.

Joekar-Niasar, V., Hassanizadeh, S.M., Dahle, H.K., 2010. Non-equilibrium effects in capillarity and interfacial area in two-phase flow: Dynamic pore-network modelling. J. Fluid Mech. 655, 38–71. https://doi.org/10.1017/S0022112010000704.

Johannessen, B., Hanslin, H., Muthanna, T., 2017. Green roof performance potential in cold and wet regions. Ecol. Eng. 106, 436–447. https://doi.org/10.1016/j.ecoleng.2017.06.011.

Kalaydjian, F., 1987. A macroscopic description of multiphase flow in porous media involving spacetime evolution of fluid/fluid interface. Transp. Porous Media 2 (6), 537–552. https://doi.org/10.1007/BF00192154.

Koch, J., Rätz, A., Schweizer, B., 2013. Two-phase flow equations with a dynamic capillary pressure. Eur. J. Appl. Math. 24 (1), 49–75. https://doi.org/10.1017/S0956792512000307.

Landry, C., Karpyn, Z., Ayala, O., 2014. Relative permeability of homogenous-wet and mixed-wet porous media as determined by pore-scale lattice boltzmann modeling. Water Resour. Res. 50 (5), 3672–3689. https://doi.org/10.1002/2013WR015148.

Latva-Kokko, M., Rothman, D., 2007. Scaling of dynamic contact angles in a lattice-boltzmann model, Physical Review Letters 98 (25). doi:10.1103/PhysRevLett.98.254503.

Li, K., Horne, R., 2006. Comparison of methods to calculate relative permeability from capillary pressure in consolidated water-wet porous media, Water Resources Research 42 (6). doi:10.1029/2005WR004482.

Li, X., Chen, S., Xu, Q., Xu, Y., 2017. Modeling the three-dimensional unsaturated water transport in concrete at the mesoscale. Computers Struct. 190, 61–74. https://doi.org/10.1016/j.compstruc.2017.05.005.

Li, Z., Galindo-Torres, S., Yan, G., Scheuermann, A., Li, L., 2018. A lattice boltzmann investigation of steady-state fluid distribution, capillary pressure and relative permeability of a porous medium: Effects of fluid and geometrical properties. Adv. Water Resour. 116, 153–166. https://doi.org/10.1016/j.advwatres.2018.04.009.

Liu, Z., Herring, A., Arns, C., Berg, S., Armstrong, R., 2017. Pore-scale characterization of two-phase flow using integral geometry. Transp. Porous Media 118 (1), 99–117. https://doi.org/10.1007/s11242-017-0849-5.

Løvoll, G., Jankov, M., Måløy, K., Toussaint, R., Schmittbuhl, J., Schäfer, G., Méheust, Y., 2011. Influence of viscous fingering on dynamic saturation-pressure curves in porous media. Transp. Porous Media 86 (1), 305–324. https://doi.org/10.1007/s11242-010-9622-8.

Lunowa, S., Bringedal, C., Pop, I., 2021. On an averaged model for immiscible two-phase flow with surface tension and dynamic contact angle in a thin strip. Studies Appl. Math. 147 (1), 84–126. https://doi.org/10.1111/sapm.12376.

Manthey, S., Hassanizadeh, S.M., Helmig, R., 2005. Macro-scale dynamic effects in homogeneous and heterogeneous porous media. Transp. Porous Media 58 (1–2), 121–145. https://doi.org/10.1007/s11242-004-5472-6.

Manthey, S., Hassanizadeh, S.M., Helmig, R., Hilfer, R., 2008. Dimensional analysis of two-phase flow including a rate-dependent capillary pressure-saturation relationship. Adv. Water Resour. 31 (9), 1137–1150. https://doi.org/10.1016/j.advwatres.2008.01.021.

Mikelić, A., 2003. On an averaged model for the 2-fluid immiscible flow with surface tension in a thin cylindrical tube. Comput. Geosci. 7 (3), 183–196. https://doi.org/10.1023/A:1025527716078.

Mikelic, A., 2010. A global existence result for the equations describing unsaturated flow in porous media with dynamic capillary pressure. J. Diff. Eqs. 248 (6), 1561–1577. https://doi.org/10.1016/j.jde.2009.11.022.

Pettersson, K., Maggiolo, D., Sasic, S., Johansson, P., Sasic-Kalagasidis, A., 2020. On the impact of porous media microstructure on rainfall infiltration of thin homogeneous

green roof growth substrates, Journal of Hydrology 582. doi:10.1016/j.jhydrol.2019.124286.
Porter, M., Schaap, M., Wildenschild, D., 2009. Lattice-boltzmann simulations of the capillary pressure-saturation-interfacial area relationship for porous media. Adv. Water Resour. 32 (11), 1632–1640. https://doi.org/10.1016/j.advwatres.2009.08.009.
Primkulov, B.K., Pahlavan, A.A., Fu, X., Zhao, B., MacMinn, C.W., Juanes, R., 2019. Signatures of fluid-fluid displacement in porous media: Wettability, patterns and pressures. J. Fluid Mech. 875, R4. https://doi.org/10.1017/jfm.2019.554.
Purcell, W., 1949. Capillary pressures - their measurement using mercury and the calculation of permeability therefrom. J. Petrol. Technol. 1 (02), 39–48. https://doi.org/10.2118/949039-G.
Qin, C.-Z., van Brummelen, H., 2019. A dynamic pore-network model for spontaneous imbibition in porous media, Advances in Water Resources 133. doi:10.1016/j.advwatres.2019.103420.
Raiskinmäki, P., Shakib-Manesh, A., Jäsberg, A., Koponen, A., Merikoski, J., Timonen, J., 2002. Lattice-boltzmann simulation of capillary rise dynamics. J. Stat. Phys. 107 (1–2), 143–158. https://doi.org/10.1023/A:1014506503793.
Sadeghi, M, Agnaou, M, Barralet, J, Gostick, J, 2020. Dispersion modeling in pore networks: A comparison of common pore-scale models and alternative approaches. J. Contam. Hydrol. 228 https://doi.org/10.1016/j.jconhyd.2019.103578.
Sbragaglia, M., Sugiyama, K., Biferale, L., 2008. Wetting failure and contact line dynamics in a couette flow. J. Fluid Mech. 614, 471–493. https://doi.org/10.1017/S0022112008003649.
Schlüter, S., Berg, S., Rücker, M., Armstrong, R., Vogel, H.-J., Hilfer, R., Wildenschild, D., 2016. Pore-scale displacement mechanisms as a source of hysteresis for two-phase flow in porous media. Water Resour. Res. 52 (3), 2194–2205. https://doi.org/10.1002/2015WR018254.
Segura, L., 2007. Modeling at pore-scale isothermal drying of porous materials: Liquid and vapor diffusivity. Drying Technol. 25 (10), 1677–1686. https://doi.org/10.1080/07373930701590889.
Shahraeeni, E., Or, D., 2012. Pore scale mechanisms for enhanced vapor transport through partially saturated porous media. Water Resources Research 48 (5). https://doi.org/10.1029/2011WR011036.
Shan, X., Chen, H., 1993. Lattice boltzmann model for simulating flows with multiple phases and components. Phys. Rev. E 47, 1815–1819. https://doi.org/10.1103/PhysRevE.47.1815.
Shokri, N., Lehmann, P., 2009. Characteristics of evaporation from partially wettable porous media. Water Resources Research 45 (2). https://doi.org/10.1029/2008WR007185.
Siltecho, S., Hammecker, C., Sriboonlue, V., Clermont-Dauphin, C., Trelo-Ges, V., Antonino, A., Angulo-Jaramillo, R., 2015. Use of field and laboratory methods for estimating unsaturated hydraulic properties under different land uses. Hydrol. Earth Syst. Sci. 19 (3), 1193–1207. https://doi.org/10.5194/hess-19-1193-2015.
Soltani, A., Azimi, M., Deng, A., Taheri, A., 2019. A simplified method for determination of the soil-water characteristic curve variables. Int. J. Geotech. Eng. 13 (4), 316–325. https://doi.org/10.1080/19386362.2017.1344450.
Succi, S., 2001. The lattice Boltzmann equation: for fluid dynamics and beyond. Oxford University Press.
Suh, H.S., Kang, D.H., Jang, J., Kim, K.Y., Yun, T.S., 2017. Capillary pressure at irregularly shaped pore throats: Implications for water retention characteristics. Adv. Water Resour. 110, 51–58. https://doi.org/10.1016/J.ADVWATRES.2017.09.025.
van Genuchten, M., 1980. Closed-form equation for predicting the hydraulic conductivity of unsaturated soils. Soil Science Soc. Am. J. 44 (5), 892–898. https://doi.org/10.2136/sssaj1980.03615995004400050002x.
Vogel, H.-J., Tölke, J., Schulz, V.P., Krafczyk, M., Roth, K., 2005. Comparison of a Lattice-Boltzmann Model, a Full-Morphology Model, and a Pore Network Model for Determining Capillary Pressure-Saturation Relationships. Vadose Zone J. 4 (2), 380–388. https://doi.org/10.2136/vzj2004.0114.
Washburn, E.W., 1921. The dynamics of capillary flow. Phys. Rev. 17, 273–283. https://doi.org/10.1103/PhysRev.17.273.
Wayllace, A., Lu, N., 2012. A transient water release and imbibitions method for rapidly measuring wetting and drying soil water retention and hydraulic conductivity functions, Geotechnical Testing Journal 35 (1). doi:10.1520/GTJ103596.
Weitz, D., Stokes, J., Ball, R., Kushnick, A., 1987. Dynamic capillary pressure in porous media: Origin of the viscous-fingering length scale. Phys. Rev. Lett. 59 (26), 2967–2970. https://doi.org/10.1103/PhysRevLett.59.2967.